Math. Model. Nat. Phenom.
Vol. 9, No. 6, 2014, pp. 98–116
DOI: 10.1051/mmnp/20149608

Patient-specific Blood Flow Simulations: Setting Dirichlet Boundary Conditions for Minimal Error with Respect to Measured Data

J. Tiago *[1], A. Gambaruto[2], A. Sequeira[1]

[1] Departamento de Matemática and CEMAT/IST Instituto Superior Técnico, Universidade de Lisboa
Av. Rovisco Pais 1, 1049-001 Lisboa, Portugal

[2] Computer Applications in Science & Engineering (CASE), Barcelona Supercomputing Center
Nexus I - Campus Nord UPC, C/ Jordi Girona 2, 3a. Planta, 08034 Barcelona, Spain

Abstract. We present a fully automatic approach to recover boundary conditions and locations of the vessel wall, given a crude initial guess and some velocity cross-sections, which can be corrupted by noise. This paper contributes to the body of work regarding patient-specific numerical simulations of blood flow, where the computational domain and boundary conditions have an implicit uncertainty and error, that derives from acquiring and processing clinical data in the form of medical images. The tools described in this paper fit well in the current approach of performing patient-specific simulations, where a reasonable segmentation of the medical images is used to form the computational domain, and boundary conditions are obtained as velocity cross-sections from phase-contrast magnetic resonance imaging. The only additional requirement in the proposed methods is to obtain additional velocity cross-section measurements throughout the domain. The tools developed around optimal control theory, would then minimize a user defined cost function to fit the observations, while solving the incompressible Navier-Stokes equations. Examples include two-dimensional idealized geometries and an anatomically realistic saccular geometry description.

Keywords and phrases: boundary control, error minimization, patient-specific, computational hemodynamics, domain uncertainty, boundary condition uncertainty

Mathematics Subject Classification: 76B75, 76D05, 76D55, 76M10

1. Introduction

Recent years have seen the rapid development of technology and especially computer hardware, that has allowed for an equally rapid development of numerical methods to simulate a large variety of physical phenomena. This has proved to be a viable means to readily provide accurate solutions of complex problems. The accuracy of the simulations is however limited to our ability to model the physical phenomena, not only in the formulation of the mathematical equations, but also in the setup definition of the problem which includes setting coefficients and boundary conditions. In this work we specifically consider

*Corresponding author. E-mail: jftiago@math.ist.utl.pt

uncertainty associated to numerical simulations of patient-specific blood flow, however the methodology can naturally be extended to other flow problems.

Another important technological development of the last few years has been in medical devices, including medical imaging. Patient-specific studies using non-invasive clinical imaging data, that can be acquired as part of current medical protocols, have become routine in the research community. Such numerical simulations have played a part in further understanding many cardiovascular diseases due to the accurate and high resolution computed solution. It has enabled researchers to probe, query and observe complex and coupled phenomena based on the mathematical models. The validation of numerical simulations of patient-specific studies largely remains an open problem as there is no means for accurate benchmarking for a given clinically acquired dataset. Hence, while the complexity of problems being modeled has increased with greater sophistication in the mathematical description, used to build a more realistic behavior of human physiology, the possibility of feasibly bracketing errors, due to model or setup uncertainty, has grown more difficult and unattainable.

The imaging data, from which patient-specific studies are built upon, are acquired from non-invasive (or minimally-invasive) medical imaging, such as magnetic resonance imaging (MRI) or computed tomography (CT), with or without contrast. To some extent, also Doppler ultrasound can be used, though it is generally of lower resolution. These data sets contain errors typically in the form of noise and limited resolution, and a multitude of artifacts and signal degradation can occur (cf. [1, 28, 37]). Sophisticated image processing may be used to reconstruct a 3-dimensional computational model. It has been seen however, that a substantially different choice in the image processing method will give different results. The reconstructed geometry hence varies, with no way of knowing what is the ground truth.

Several studies ([4, 14, 17, 25]) have looked at variability in the reconstructed geometry definition and reported differences in physiologically relevant measures associated to disease (typically the wall shear stress and derived measures). In a similar fashion, there is uncertainty regarding which rheological model for blood to choose [16,23], appropriate inflow/outflow boundary conditions to set [26,30] and parameters for the structural models describing the vessel lumen and surrounding tissue [24, 27, 35]. Uncertainties can be mitigated by sampling the parameter space, estimating therefore error bounds. While this is unfeasible for a general problem, due to high computational costs, a subset of relevant measures can be investigated in order to obtain credible results and correlations to disease descriptors [14]. Such selective sampling of the parameter space often requires human intervention and remains subjective. A preferred approach would be to have an automatic method to obtain the unique solution that minimizes an error cost function, based on some extra observations obtained from clinical imaging data. Such solution can help setting the parameters for the numerical simulations.

We take this as our starting point and motivation for the current work. The simulation methodology presented in this paper assures the minimization of error in the solution, that can be associated to any form of uncertainty in translating the clinical data to a computational domain and setup. The approach is suitable for patient-specific studies and needs two forms of data: i) a stack of medical images (e.g. CT or MRI) from which to reconstruct an approximate computational domain; ii) and a few cross-sectional velocity contours, that can be obtained from phase-contrast magnetic resonance imaging (PC-MRI), which can be corrupted due to noise or limited resolution. Once we assume this, a misfit between the measured velocity data and the computed solution is minimized. This implies a control of the velocity values at the boundary of the approximated computational domain. Optimal control techniques in cardiovascular modeling have been used recently in the frame of Data Assimilation (DA) (cf. [7, 8, 19]). Although our approach allows the velocity profile reconstruction (the subject of DA), we are mainly interested in reducing the uncertainty associated to the reconstructed domain.

The work presented in this paper outlines the methodology with application to 2-dimensional problems, with more realistic 3-dimensional cases as scope for future work. For each case, a ground truth solution is generated in order to compare and evaluate the minimal error solution obtained from an optimal control methodology. The cases studied are presented in order of increasing complexity.

The control parameters are the velocity Dirichlet conditions that describe both the truncated domain inflow sections and the geometry wall. The outflows are given by a traction-free (Neumann) condition and are not a parameter in the optimal control, but remain a solution of the Navier-Stokes equations. An initial guess solution for the optimal control problem is arbitrary, and given here as an average velocity flow field, however, other easily available options including a uniform zero-velocity field and the solution of the flow field in the approximate computational domain, can also be tested.

The organization of the paper reads as follows. In Section 2 we briefly recall the mathematical models commonly used to model blood flow in the vascular system and we introduce the boundary control problem that we will use as a tool to reconstruct the blood profile in the approximated geometries. Next, in Section 3, we describe the numerical approach to solve the optimal control problem. Finally, we present in Section 4 the numerical results obtained for different idealized geometries.

2. Mathematical model and control problem

2.1. Mathematical model for blood flow

In this section we assume that Ω represents the fluid domain, which corresponds to the lumen of the artery, as shown in Figure 1. The boundary of Ω consists of the artery interior wall, represented by Γ_{wall}, and two artificial boundaries Γ_{in} and Γ_{out} to truncate the domain from the whole system. We also call Γ_{in} the inlet which corresponds to the proximal section, where the average mean flow is negative with respect to the section outward-pointing normal direction. As to Γ_{out}, we also call it the outlet which corresponds to the distal section, where the average mean flow is positive with respect to the section outward-pointing normal direction.

From the linear momentum and mass conservation equations we can derive the blood flow model. For our purposes we assume blood to be an isothermal, viscous and incompressible fluid. Hence we obtain the equations

$$\begin{cases} \rho\big(\dfrac{\partial \mathbf{u}}{\partial t} + (\mathbf{u}\cdot\nabla)\mathbf{u}\big) - div\,\tau + \nabla p = \mathbf{f} & \text{in } \Omega \\ div\,\mathbf{u} = 0 & \text{in } \Omega \end{cases} \tag{2.1}$$

where the stress tensor τ is given by the constitutive equation

$$\tau = 2\mu D\mathbf{u}, \quad \text{where } D\mathbf{u} = \frac{\nabla\mathbf{u} + \nabla\mathbf{u}^T}{2}.$$

The dynamic viscosity μ can be considered either as constant or as shear rate dependent. In fact, blood may present a shear-thinning behavior which can only be accurately represented using a non-Newtonian model in which the viscosity is no longer a constant; see for instance [31]. Since here our main focus is the

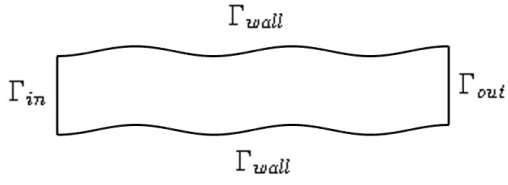

FIGURE 1. Representation of the domain Ω

recovery of accurate boundary conditions and the vessel wall, to simplify, we assume that the viscosity is constant and blood is modeled as a Newtonian fluid by the well known Navier-Stokes equations.

In order to close system (2.1) and obtain a well posed model, we fix the velocity to be zero at Γ_{wall} and we impose the so-called homogeneous Neumann boundary conditions

$$(-p\mathbf{I} + 2\mu D\mathbf{u}) \cdot \mathbf{n} = 0 \quad \text{on } \Gamma_{out}.$$

Here $\mathbf{n}$ represents the exterior unit normal vector to the surface and $\mathbf{I}$ the identity matrix. Finally, we fix a velocity profile at the inlet Γ_{in}. The right hand side of the balance of the momentum is only composed by the constant gravity force, which can be considered as part of the pressure p by a suitable change of variables. Therefore, for simplicity, we can consider it to be $f = \mathbf{0}$. Furthermore, we will only deal with the stationary model, neglecting therefore the time dependence. For more details on the mathematical modeling of blood flow we refer to [29].

2.2. The optimal control problem

As mentioned in the Introduction, there is an inherent uncertainty when performing patient-specific numerical simulations. In order to obtain some indicative measure of error bounds, one approach consists in sampling the uncertainty parameter space to carry out the study. When dealing with the uncertainty associated to the geometry reconstruction, the parameter space can be prohibitively large. Here we propose a less computationally intensive approach based on an optimal control problem.

The inlet velocity profile at the artificial boundary condition Γ_{in}, and the location of the no-slip boundary condition that defines the reconstructed wall Γ_{wall}, are often indicated as key measures that propagate to the solution of equation (2.1). This is especially relevant when considering fluid mechanics measures with physiological interest, such as the wall shear stress [13, 15]. A good criterion to set the correct Dirichlet boundary conditions is therefore imperative.

In order to perform a comparison of different boundary conditions we must accept that some data of the true solution itself is available (even if corrupted by noise). Here we assume to know the velocity profile on some sections of the lumen, possibly obtained very close to the boundary wall. We take Ω_{obs} to represent the union of such observed sections, and $\mathbf{u}_d$ the known velocity data on these sections. Let us denote by Ω the reconstructed domain, obtained from medical images, which lies close to the true domain Ω_0. Let us represent the boundary for which we want to calibrate the velocity profile by Γ_c. In practice this boundary may consist in part or whole of Γ_{wall} and/or the inlet Γ_{in}. This allows for a great flexibility in the method.

We can now choose the uncertain velocity profiles as the solution of the optimal control problem

$$\min_{\mathbf{c}\in\mathcal{A}} \mathbf{J}(\mathbf{c}) = \alpha_1 \int_{\Omega_{obs}} |\mathbf{u} - \mathbf{u}_d|^2 \, dx + \alpha_2 \int_{\Gamma_c} |\nabla_s \mathbf{c}|^2 \, ds \tag{2.2}$$

subject to

$$\begin{cases} -div\,\tau + \rho(\mathbf{u}\cdot\nabla)\mathbf{u} + \nabla p = 0 \text{ in } \Omega \\ div\,\mathbf{u} = 0 \qquad\qquad\qquad\qquad \text{in } \Omega, \\ \mathbf{u} = 0 \qquad\qquad\qquad\qquad\quad \text{on } \Gamma_{wall} \setminus \Gamma_c \\ \mathbf{u} = \mathbf{c} \qquad\qquad\qquad\qquad\quad \text{on } \Gamma_c \\ (-p\mathbf{I} + 2\mu D\mathbf{u}) \cdot \mathbf{n} = 0 \qquad \text{on } \Gamma_{out}. \end{cases} \tag{2.3}$$

The variable $\mathbf{c}$ stands for the control vector function, consisting in the unknown velocity profiles at the different parts of Γ_c. The term α_2 weighting the tangential gradient $\nabla_s \mathbf{c}$ is a regularization term (see [21]). In practice, we can also choose $\mathbf{c}$ to have lower dimension than the velocity vector through a parametrization. Such parametrization could, for example, be a polynomial function, hence a spatial

correlation of the point values of Γ_c. We will give more details in Section 4. The admissible set $\mathcal{A}$ refers to the admissible function space for the control function plus other bound type constraints for the control. While the minimization of the first term in (2.2) clearly leads to an approximation of the computed velocity to the data, the second term is no less important. Besides the contribution of this term to a more regular solution, it suffices to ensure the uniqueness of solution for the optimal control problem associated to the linearization of (2.3). Also, at the discrete level, it avoids the presence of spurious minimum [3, 20]. The weights α_1, α_2 should be positive and balanced in such a way that priority should be given to minimizing the difference rather than obtaining a zero gradient of the control function.

With regards to the well-posedness of the control problem (2.2)-(2.3), it is not clear yet, with such a general setting, if it is possible to prove the existence of solution. The main issue is the arbitrariness of the sections composing Ω_{obs}. This question was treated for similar problems, in [9–11], but for the case $\Omega_{obs} = \Omega$ which cannot be applied to our case. We do not treat this important issue here, rather we validate this approach with several numerical experiments.

3. Discretization and numerical approach

The solution of problem (2.2)-(2.3) can be obtained numerically. To this purpose we adopt a direct approach also known as the Discretize then Optimize (DO) approach, consisting in two stages. First the optimal control problem is discretized, then the resulting non-linear mathematical programming problem is solved. To this end, we begin by writing the steady weak formulation of the state equation.

3.1. Galerkin formulation and discretization

Let us consider the classical variational formulation of problem (2.3): Find $u \in V_0$ and $p \in Q_0$ such that

$$\begin{cases} \int\limits_{\Omega} \tau : \nabla \mathbf{v} + \int\limits_{\Omega} (\rho(\mathbf{u} \cdot \nabla)\mathbf{u}) \cdot \mathbf{v} - \int\limits_{\Omega} p \, div \, \mathbf{v} = 0 \\ \int\limits_{\Omega} q \, div \, \mathbf{u} = 0 \end{cases} \tag{3.1}$$

for all $\mathbf{v} \in \mathbf{V}$ and $q \in Q$.

The function spaces $\mathbf{V}$ and Q depend on the Hilbert spaces $\mathbf{V}_0$ and Q_0 where $\mathbf{u}$ and $\mathbf{p}$ are defined. However the test functions should verify $\mathbf{v} = 0$ on $\Gamma_{in} \cup \Gamma_{wall}$. An example for those spaces is $\mathbf{V}_0 = \mathbf{H}^1(\Omega)$ and $Q_0 = L^2(\Omega)$. For more details see for instance [18]. We then consider the finite dimensional subspaces $\mathbf{V}_h \subset \mathbf{V}$ and $Q_h \subset Q$ with $h > 0$, $dim(\mathbf{V}_h) = N_u$, $dim(Q_h) = N_p$ and take the finite dimensional approximations

$$\mathbf{u}_h = \sum_{j=1}^{N_u} u_j \phi_j \in \mathbf{V}_h, \quad p_h = \sum_{k=1}^{N_p} p_k \psi_k \in Q_h \tag{3.2}$$

with $\phi_j \in \mathbf{V}_h$ and $\psi_k \in Q_h$. Again we refer to [18] for the choice of such spaces. In this work we adopt the finite element method and typical spaces $\mathbf{V}_h$ and Q_h corresponding to the Taylor-Hood elements ($P2$-$P1$).

Let us now replace both $\mathbf{u}$, $\mathbf{p}$ by their finite dimensional approximations in (3.1). Also we replace the corresponding test functions by ϕ_i, $i = 1...N_u$ and ψ_i, $i = 1...N_p$. Starting with the convective term, we obtain the vector

$$\int\limits_{\Omega} \left[\left(\rho \sum_{j=1}^{N_u} u_j \phi_j \cdot \nabla \right) \sum_{k=1}^{N_u} u_k \phi_k \cdot \phi_i \right], \; i = 1...N_u$$

that can be written as

$$\mathbf{N}(U)U = \left(\sum_{j=1}^{N_u} u_j \sum_{k=1}^{N_u} u_k \int\limits_{\Omega} (\rho \phi_j \cdot \nabla)\phi_k \cdot \phi_i \right)_{i=1...N_u}$$

where $U = (u_1, ..., u_{N_u})^T$ and

$$(\mathbf{N}(U))_{i,j} = \sum_{k=1}^{N_u} u_k \int_\Omega (\rho\phi_j \cdot \nabla)\phi_k \cdot \phi_i \, .$$

As for the term corresponding to the viscous stress tensor τ, we obtain

$$\left(\sum_{k=1}^{N_u} \mathbf{u}_k \int_\Omega 2\mu D\phi_k : \nabla\phi_i \right)_{i=1...N_u} = \mathbf{S}U \, .$$

Similary, we discretize the pressure term as $\mathbf{B}^T P$, with $P = (p_1, ..., p_{N_p})^T$, and we obtain the discrete version of system (3.1), given by

$$\begin{cases} \mathbf{S}U + \mathbf{N}(U)U + \mathbf{B}^T P = 0 \\ \mathbf{B}U = 0 \, . \end{cases} \tag{3.3}$$

The cost function (2.2) can also be discretized using the same approximation spaces. Let us fix $(\phi_i)_{i=1...N_o}$ to be the basis functions associated to the nodes in Ω_{obs}. Similarly, let $(\phi_i)_{i=1...N_c}$ be the basis functions associated to Γ_c and set the approximated control function as

$$\mathbf{c}_h = \sum_{j=1}^{N_c} c_j \phi_j \, .$$

We can now replace the functions in (2.2) by their approximations

$$\mathbf{u}_h, \, \mathbf{c}_h \text{ and } \mathbf{u}_{h_d} = \sum_{i=1}^{N_0} u_{d_i} \phi_i$$

obtaining

$$\begin{aligned} &\alpha_1 \int_{\Omega_{obs}} \left\langle \sum_i^{N_o} (u_i - u_{di})\phi_i, \sum_j^{N_o} (u_j - u_{dj})\phi_j \right\rangle dx + \alpha_2 \int_{\Gamma_c} \left\langle \sum_{i=1}^{N_c} c_i \nabla_s \phi_i, \sum_{j=1}^{N_c} c_j \nabla_s \phi_j \right\rangle ds \\ &= \sum_i^{N_o} (u_i - u_{di}) \sum_j^{N_o} (u_j - u_{di}) \int_{\Omega_{obs}} \alpha_1 \langle \phi_i, \phi_j \rangle \, dx + \sum_{i=1}^{N_c} c_i \sum_{j=1}^{N_c} c_j \int_{\Gamma_c} \alpha_2 \langle \nabla_s \phi_i, \nabla_s \phi_j \rangle \, ds \\ &= (U - U_d)^T \mathbf{M} (U - U_d) + C^T \mathbf{W} C \\ &= \left\langle (U - U_d)^T, (U - U_d) \right\rangle_{\mathbf{M}} + \left\langle C^T, C \right\rangle_{\mathbf{W}} \\ &= \|U - U_d\|^2_{N_u} + \|C\|^2_{N_c} \end{aligned} \tag{3.4}$$

where the matrices $\mathbf{M}$ and $\mathbf{W}$ have dimension $N_u \times N_u$ and $N_c \times N_c$, respectively, and $U_d \in R^{N_u}$ is an extension of $(u_{di})_{i=1...N_o}$. Both $\mathbf{M}$ and U_d have zero components for the positions associated to elements outside of Ω_{obs}. The norm $\| \cdot \|_{N_u}$, is the norm induced by the inner product $< \cdot, \cdot >_{\mathbf{M}}$ and $\| \cdot \|_{N_c}$ the norm obtained from $< \cdot, \cdot >_{\mathbf{W}}$.

Taking into account (3.3) and (3.4), the discrete version of the control problem (2.2)-(2.3) becomes

$$\min_{C \in \mathbf{A}} J(U(C), C) = \|U - U_d\|^2_{N_u} + \|C\|^2_{N_c} \tag{3.5}$$

subject to

$$\begin{cases} \mathbf{S}(\bar{U}, C) + \mathbf{N}(\bar{U}, C)\,(\bar{U}, C) + B^T P = 0 \\ B(\bar{U}, C) = 0 \end{cases} \tag{3.6}$$

where we assumed $U = (\bar{U}, C)$ with $\bar{U}$ representing the non-controlled velocity coefficients and $\mathbf{A}$ represents the admissible set for the coefficients of C.

If we assume that $\mathbf{A}$ can be described using inequality constraints and take $F(C) = J(U(C), C)$, then problem (3.5)-(3.6) can be written as

$$\min_C F(C) \tag{3.7}$$

$$H(C) \geq 0 \tag{3.8}$$

which is a non-linear mathematical programming problem.

3.2. Resolution of the non-linear optimization problem

When using the Discretize then Optimize approach, the main issue is the resolution of the non-linear mathematical programming problem (3.7)-(3.8). To do this, we adopt the Sequential Quadratic Programming (SQP) approach. It consists in two main stages. In the first one we need to approximate the non-linear problem by a quadratic programming problem (QP). This is done by linearizing the constraints (3.8) around a fixed estimate for the control and by obtaining a second order approximation to the modified Lagrangian associated to (3.7)-(3.8). The second stage consists in solving (QP) to obtain a descent direction for the non-linear problem and to use it, to obtain the next approximate solution, after applying a line search method. Such solution satisfies the linearized constraints, and converges to a solution satisfying the nonlinear constraints and the first-order optimality conditions for the nonlinear problem, up to certain given feasibility and optimality tolerances, respectively.

We now describe the algorithm for the used SQP approach, which corresponds to the SNOPT implementation. The interested reader is referred to [22] for further details.

First let us assume that the solution $\hat{C}$ of (3.7)-(3.8) verifies the KKT optimality conditions

$$\begin{cases} DH(\hat{C})^T\lambda = DF(\hat{C}) \\ H(\hat{C})^T\lambda = 0 \\ H(\hat{C}) \geq 0 \\ \lambda \geq 0 \end{cases}$$

where DF and DH are the gradients of F and H, respectively, and λ is the vector of the Lagrange multipliers.

We can then summarize the algorithm as follows:

1. Fix C_k as an admissible estimate for the minimizer, and λ_k as the corresponding vector of multipliers;
2. Determine $\mathcal{H}_k$, the Hessian (or a quasi-Newton approximation) of the modified Lagrangian

$$\mathcal{L}(C, C_k, \lambda_k) = F(C) - \lambda_k^T[H(C_k) - C_k - DH(C_k)(C - C_k)];$$

3. Solve the Linear Quadratic problem

$$\begin{aligned} &\min_C \mathcal{Q}(C, C_k, \lambda_k) = F(C_k) + DF^T(C_k)(C - C_k) - \frac{1}{2}(C - C_k)^T\mathcal{H}_k(C - C_k) \\ &C_k + DH(C_k)(C - C_k) \geq 0 \end{aligned} \tag{3.9}$$

   to obtain the optimal $(\bar{C}_k, \bar{\lambda}_k, \bar{s}_k)$, where $\hat{s}_k$ is the vector of the slack variables associated to the linear constraints in (3.9);
4. Find $\alpha_{k+1} \in (0, 1]$ so that the merit function

$$M_\gamma(C, \lambda, s) = F(C) + \lambda^T(H(C) - s) + \frac{1}{2}\sum_{i=1}^{m}\gamma_i(H_i(C) - s_i)^2$$

decreases along the line

$$d(\alpha) = (C_k, \lambda_k, s_k) + \alpha[(\bar{C}_k, \bar{\lambda}_k, \bar{s}_k) - (C_k, \lambda_k, s_k)],$$

where $s_i\, i = 1...m$ are the components of s and γ is a vector of penalty parameters (see [22] for details on how to choose γ). Then set $(C_{k+1}, \lambda_{k+1}, s_{k+1}) = d(\alpha_{k+1})$;

5. Check if the optimality tolerance is satisfied. If not, go to step one and repeat.

Remark 3.1. It is important to remark that during the procedure outlined above, every time that $F(C) = J(U(C), C)$ is evaluated, the vector U must be found by solving the discretized Navier-Stokes equations given by system (3.6), where C corresponds to the discretized velocity profile on Γ_c. This can be done by a Newton type method together with a suitable linear solver.

4. Numerical experiments

In this section we present the numerical results of the procedure introduced above. To this end we considered several 2-dimensional idealized geometries representing longitudinal sections of blood vessels. Before presenting the results, a summary of the procedure is detailed in order to emphasize the analogy to data obtained from a practical clinical setting, and provide a step-by-step explanation of how the results were obtained and how they should be analyzed:

i) *Fix a domain Ω_o and generate a solution which will be considered the reference true solution.*
At the inlet of the vessel, we considered a characteristic radius of $R = 0.31\,cm$. For the blood model (2.1) we considered $\rho = 1050\,kg/m^3$, $\mu = 0.0036\,Pa \cdot s$. All the solutions, taken as reference solutions, were generated by solving the blood model using a parabolic inlet profile corresponding to a flow rate of $Q = 1.95\,cm^3 s^{-1}$. This results in $Re \approx 117$. These parameters were used in [2] where Newtonian and non-Newtonian effects were compared for blood flow. As to the boundary walls and the outlet, we used no-slip and Neumann conditions, respectively, as described in Section 2.3.

ii) *Record the solution at $\Omega_{obs} \subset \Omega_o$ into a data vector $\mathbf{u}_d$.*
It is likely that this data will include noise. We simulate this situation in one example (see Section 4.3). Phase-contrast magnetic resonance imaging, that can provide velocity measurements of blood flow in arteries non-invasively, is prone to noise and limited resolution.

iii) *Consider an approximated geometry Ω as the reconstruction of Ω_0, and rename $\Omega_{obs} \cap \Omega$ as Ω_{obs}.*
In current practices of performing patient-specific computational hemodynamics, the reconstructed geometry from medical images, obtained by careful image processing and segmentation techniques, would, in general, give more reliable approximations than the extreme cases that we analyze here. The approximation Ω may not necessarily include nor be included in Ω_0. We give an idealized example for this case (see Section 4.4).

iv) *Choose the boundaries to control, the corresponding control variables and its constraints.*
This step depends on each situation. In particular, the a priori knowledge of some features about the solution may help to define Γ_c, $\mathbf{c}$ and $\mathcal{A}$. For instance, if we can assume that the velocity at the controlled boundary follows a certain known profile $P(x, y)$, then we can reduce the dimension of the control variable to a set of control parameters. This is the case when we are trying to adjust the velocity vector at the inlet where it is assumed to be a parabolic profile $P(y)$. In this case, the control variable reduces to parameter c adjusting the maximum velocity. In this case the corresponding integral term in (2.2) vanishes.

v) *Solve problem (2.2)-(2.3) numerically.*
We discretize the optimal control problem to obtain a problem of the type (3.7)-(3.8). This was done using the finite element discretization implemented in Comsol Multiphysics ([5]), based on the P2-P1 elements. The values of the parameters α_1 and α_2 can be obtained by different techniques. A possibility could be the discrepancy principle, which could be computationally expensive when applied to problem (2.2-2.3). Here we took $\alpha_1 = 10^6$ and $\alpha_2 = 10^{-3}$ based on the experiments made in [19],

for similar approaches. We then use the SQP approach as described in Section 3.2. For that we used the SNOPT implementation ([22]), with feasibility and optimality tolerances both equal to 10^{-6}. As to the computation of $F(C) = J(U(C), C)$, we used the damped Newton method ([12]) together with the direct linear solver PARDISO ([32]).

vi) *Analysis of the results.*
In the regions where the cross sections of Ω_0 are fully contained in Ω we expect to see areas of small velocity magnitude reproducing the no-slip conditions on Ω_0. Beyond that, in $\Omega \setminus \Omega_0$, the velocity profile does not have any relevant physical meaning. As for the regions where the cross sections of Ω_0 lie outside of Ω, we should expect the velocity profile to coincide, up to certain error, with the profile at the corresponding regions of Ω_0.

4.1. Wavy channel

Our first example consists in a simple case where we can test some features of our procedure. Let us consider the geometry represented on the left of the top row of Figure 2. It represents a channel with perturbed boundary, with the inlet Γ_{in} at the left vertical boundary and the outlet Γ_{out} at the right vertical boundary. The wavy vessel walls that delineate the top and bottom of the domain, represent a non-trivial idealization of a 2D section of an artery. We denote it as Γ_{wall}. As mentioned above, we generate a solution with a parabolic profile on Γ_{in} corresponding to a flow rate of $Q = 1.95\, cm^3 s^{-1}$. The streamlines and axial component of the velocity for this solution are represented on the left hand side of the second row. We take this to be our true solution, and the channel as our true domain Ω_0. We assume a rough reconstruction of Ω_0 and obtain Ω, the domain represented on the right hand side of the top row. The true solution is only known by the velocity profile $\mathbf{u}_d$ over the blue lines represented in both domains in the top row of the figure. These sections correspond therefore to the observed domain Ω_{obs}. We also assume that the flow rate at the inlet boundary is known. Our first goal consists in adjusting the velocity profiles on Γ_{wall}, and on the inlet, so that the corresponding solution minimizes the difference with $\mathbf{u}_d$ over Ω_{obs}. We note that, since the observations were taken close to the wall of Ω_0, and seeing that Ω is larger than Ω_0, it is likely that the velocity vectors in Ω should have small magnitude values over the regions corresponding to the wall of Ω_0.

In this case, $\Gamma_c = \Gamma_{c_0} \cup \Gamma_{c_1} \cup \Gamma_{c_2}$ where $\Gamma_{c_0} = \Gamma_{in}$, Γ_{c_1} denotes the top wall of the vessel, and Γ_{c_2} the bottom one. In order to simplify the control variable $\mathbf{c}_0$, associated to Γ_{in}, we assume that the inlet velocity profile fits the expression

$$\mathbf{u} = \begin{pmatrix} P_{c_0}(y) \\ 0 \end{pmatrix} = \begin{pmatrix} u_{av} \dfrac{c_0+1}{c_0} \Big[1 - \Big(\dfrac{|y-R|}{R} \Big)^{c_0} \Big] \\ 0 \end{pmatrix}.$$

Keeping the average velocity u_{av} fixed ensures that the flow rate Q is preserved on the inlet boundary, with length $L = 2R$, for any positive parameter c_0. We remark that the shape of the profile varies from a piecewise linear non-smooth profile, when $c_0 = 1$, to an almost flat profile, when $c_0 = 9$. For more details see [34]. The velocity profile at Γ_{c_0} is then fully determined by the control parameter $c_0 \in [1, 9]$, and consequently, the part of the regularization term in (4), associated to Γ_{c_0}, is meaningless. As for the control variables $\mathbf{c}_1$ and $\mathbf{c}_2$, we fix them to represent the velocity vector at the corresponding boundaries. Therefore, the regularization term can be decomposed into

$$\int_{\Gamma_{c_1}} |\nabla_s \mathbf{c_1}|^2 \, ds + \int_{\Gamma_{c_2}} |\nabla_s \mathbf{c_2}|^2 \, ds \,. \tag{4.1}$$

We also use a simple constant extrapolation of $\mathbf{u}_d$ to constrain the wall controls on the outlet. These constraints will restrict the admissible set $\mathcal{A}$ to a smaller, yet reasonable, set of solutions.

As initial guess, we consider the solution generated by solving the model with $c_0 = 1$ and the control functions $\mathbf{c}_1$ and $\mathbf{c}_2$ equal to an extrapolation of $\mathbf{u}_d$. This solution is represented on the right hand side of the second row of Figure 2.

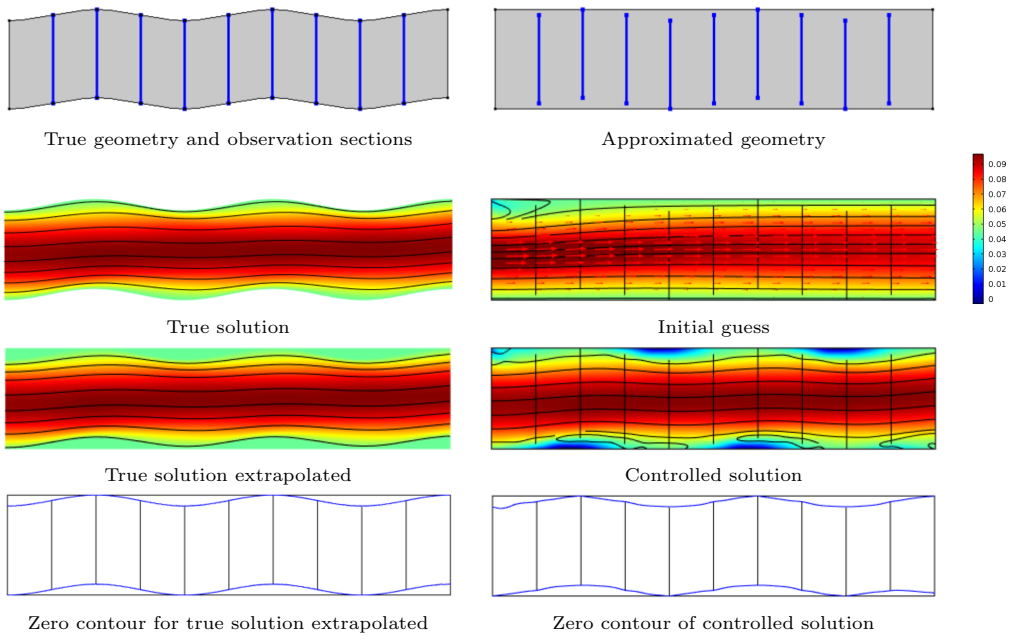

FIGURE 2. Top row left: original geometry with observed sections. Top row right: approximated geometry with observed sections. Second row left: solution for the original geometry. Second row right: approximated solution using constant average velocity. Third row left: solution extrapolated for the approximated geometry. Third row right: controlled solution. Bottom row left: zero contour level in the approximated geometry. Bottom row right: zero contour level of the controlled solution.

To solve the control problem we use 805 degrees of freedom (dofs) for the control variable approximation, 14498 dofs for the velocity and 1872 dofs for the pressure. The relative error measured over Γ_{obs}, for the initial estimate, is 0.12826. In Table 1 we represent the computational output obtained for optimality tolerances of 10^{-2}, 10^{-3} and 10^{-4}. It includes the number of major iterations of the SQP algorithm and also the accumulated number of minor iterations needed to solve each QP (3.9).

TABLE 1. Outline of computational cost for the wavy channel example, for varying optimal control tolerance.

Optimal Control Tolerance	Initial Cost	Final Cost	Relative Error	Computational Time [/min]	Major Iterations	Accumulated Minor Iterations
10^{-2}	4.69259	0.02958	0.00456	30	926	1724
10^{-3}	4.69259	0.02792	0.00378	49	1353	2151
10^{-4}	4.69259	0.02751	0.00374	61	1506	2303

The solution corresponding to the controlled boundaries is represented on the right hand side of the third row. For comparison purposes we present, on the left hand side, the true solution on top of the approximated domain, for which a simple constant extrapolation with no physical meaning is presented when Ω is larger than Ω_0. We can observe that the streamlines of the controlled solution behave as the true solution. In the bottom row, we compare the zero-velocity magnitude contour level, for both solutions. Since the zero contour level can indicate where the no-slip boundary conditions are verified by

the true solution, we can see that the controlled solution gives a way to recover the location of the wall boundary for the original domain Ω_0.

4.2. Wavy channel - non-uniform sampling

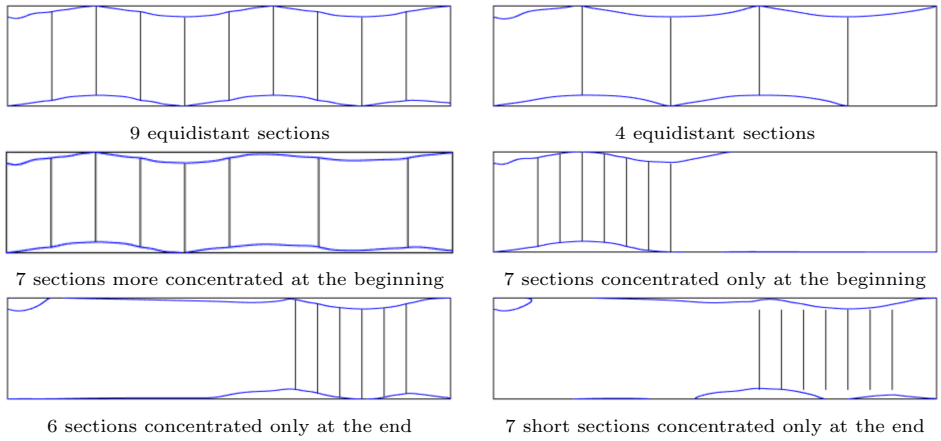

FIGURE 3. Effect of number and distribution of observed sections Ω_{obs}. The sections and location of the no-slip contour (i.e. where the velocity is zero) are shown. The true solution is presented in Figure 2.

The observations set Ω_{obs} plays an important role. In fact, as we will see next, the number and distribution of the sections where $\mathbf{u}_d$ is taken have a large impact on the accuracy of the recovered solution. In Figure 3 we present the results obtained for different Ω_{obs}.

We take, as a reference for comparison, the solution using nine observation sections, that has been previously computed as described above. As a measure of accuracy we focus on recovering the wavy wall geometry, hence the zero-velocity iso-contour that is the no-slip boundary, which is a sensitive measure and is used to evidentiate an important feature of the desired solution. On reducing the number of observation sections to four, a loss of accuracy is noticeable. By adding a higher concentration upstream, the accuracy is improved both in the region of increased number observations and downstream of it. Taking this idea further we test only sampling the upstream portion of the section very finely, however we notice that the while locally the solution has increased accuracy, elsewhere in the domain the solution is very poor. In fact, the control acted to minimize the misfit at the beginning of the channel while remaining flat closer to the outlet. This effect is independent of the region and similar results are obtained when the higher sampling is located towards the outlet. Finally we test the effect of shorter sections and note that this does not necessarily imply less accuracy.

We learn from these numerical experiments that it is important to sample the domain uniformly. Increased spatial sampling can only improve the solution locally, and likely also in the regional neighborhood. A partial set of samples, such as shorter observation cross-sections, does not directly imply a reduced accuracy.

4.3. Wavy channel - noisy observations

Our next example investigates how the solution of the control problem can be affected by the presence of noise in the data $\mathbf{u}_d$. Noise is added to the velocity profiles, and this corrupted data is taken as our initial Ω_{obs}. We use two intensity Gaussian white noise samples generated such that 99.7 percent (hence 3σ) of the values lie on the (normalized) intervals $u_{av} \times [-0.1, 0.1]$ and $u_{av} \times [-0.2, 0.2]$, respectively. Depending on the imaging modality, forms of noise will typically be Poisson or Gaussian, however artifacts may also

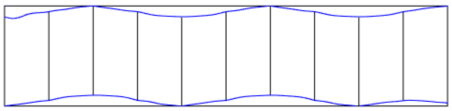

Controlled solution without noise

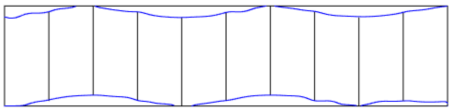

Controlled solution with 10% of noise

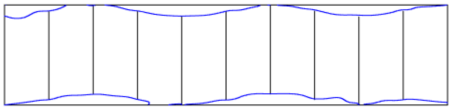

Controlled solution with 20% of noise

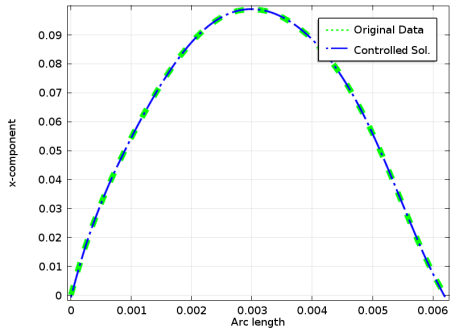

Controlled solution vs Original Data at middle section

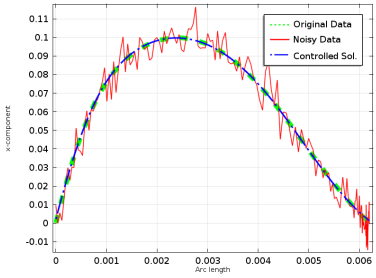

Initial section with 10% of noise

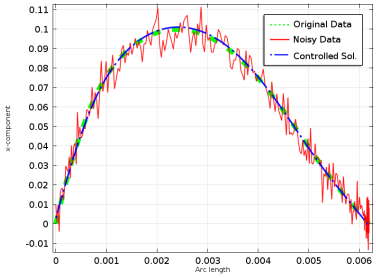

Initial section with 20% of noise

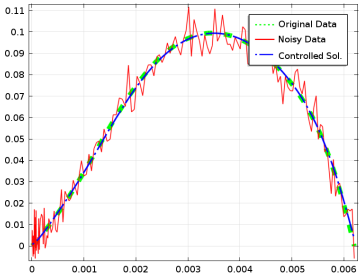

Final section with 10% of noise

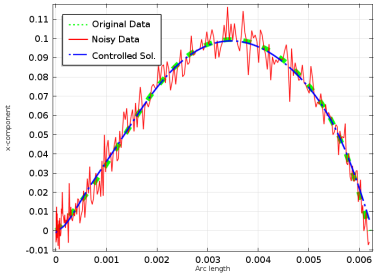

Final section with 20% of noise

FIGURE 4. Top left: comparison of the recovered zero contour levels for the case without noise on $\mathbf{u}_d$ and with 10 and 20 percent, respectively. Top right: axial component of the velocity for the true and controlled solutions on a section at the centre of the channel. Middle: comparison of the original solution with the controlled one in a section close to the inlet. Bottom: comparison of the original solution with the controlled one in a section close to the outlet.

be present and typically attributed to temporal variations. Gaussian noise is used here to represent an unbiased degradation of the measured data. Since the physical problem is modeled by the Navier-Stokes equations, which results in a smooth solution at low Reynolds numbers, it is expected that other similar forms of local random perturbations will yield comparable results. However, noise or artifacts with large spatial correlation or bias may affect the solution more than the Gaussian noise used here.

In Table 2 we show the relative errors obtained with 84614 dofs for the velocity vector and 2750 for the control variable. The noisy data, when measured over Ω_{obs}, adds a relative error to the original solution of 4% in the first case, and 8% in the second one. Even though, the controlled solution approximates the original data with a relative error smaller than 1.3% and 1.7%, respectively.

TABLE 2. Outline of computational cost for the wavy channel with noisy measurements example, for varying optimal control tolerance.

Noise Sample	Relative Error Added to Data	Relative Error of Initial Estimate	Relative Error of Controlled Solution
$u_{av} \times [-0.1, 0.1]$	0.04248	0.1292	0.0126
$u_{av} \times [-0.2, 0.2]$	0.08238	0.1292	0.0164

In Figure 4 we illustrate these results. We can see from the velocity cross-sections that the controlled solution fits accurately to the true solution profiles, shown in the figure for proximal and distal sections of the channel. The effect of the noise is more clear on the zero velocity isocontour, hence the no-slip boundary of the geometry, for the whole controlled solution: the higher level of noise can reduce the accuracy of the contour. In this example this effect is more marked on the bottom wall of the channel. Overall, a higher level of noise corruption is not seen to have a greater influence on the computed solution, with the most evident effect on the identification of the no-slip boundary, which is a sensitive measure, as mentioned above.

4.4. Wavy channel - smaller computational domain

The last test case using the wavy channel geometry consists in assuming that the reconstructed geometry Ω doesn't include the top wavy wall, hence the assumed domain is smaller than the true domain. The results for this case are shown in Figure 5. The right image in the top row shows the reduced size of the computational domain used. The optimal control problem (2.2)-(2.3) produces an accurate solution when compared to the true solution. The bottom no-slip boundary is well represented, however a way to estimate the location of the top wall for the true domain still remains to be addressed. A possible procedure to overcome this difficulty could be a sequential enlargement of Ω, until the full zero magnitude contour could be determined. Alternative high-order extrapolation could be used to give a reasonable estimate, such as using finite differences or radial basis function methods.

4.5. Stenosed channel

We now consider another simple, yet significant example. We consider a channel deformed by a stenosis typically associated to atherosclerosis, a pathology of the cardiovascular system that affects part of the population of industrialized countries. In these situations an accurate geometry definition is especially important, since measures such as the wall shear stress (WSS) are indicators for the regions of possible plaque formation (cf. [15,33]). Results for this case are presented in Figure 6. The observed domain Ω_{obs} corresponds to sections around the stenosed area to improve the local accuracy. As above, on the left hand side the reference domain and solutions are given, while on the right hand side the computed solutions using the optimal control method are presented. We can notice the increase of the velocity magnitude at the stenosis. The zero contour levels for the x-component of the velocity, shown on the bottom row, highlight how the procedure can be useful to recover the boundary in this type of geometries. The high spatial gradients of velocity formed at the stenosis are well resolved and good accuracy in recovering the no-slip contour is evident. Note that the x-component velocity is used to identify the no-slip domain, since the absolute velocity gives a poor results. Alternatively, using the y-component would also yield satisfactory results.

4.6. Wavy channel with aneurysm

We now consider a more complex example shown in Figure 7. It corresponds to a wavy channel and an aneurysm that highly deforms its upper wall. The resulting flow field is complex, with a slow recirculation region, that is in contrast to the large velocities and spatial gradients of the stenosis geometry example. The reconstructed domain Ω is taken to be a rectangular channel and a larger aneurysm (shown in the

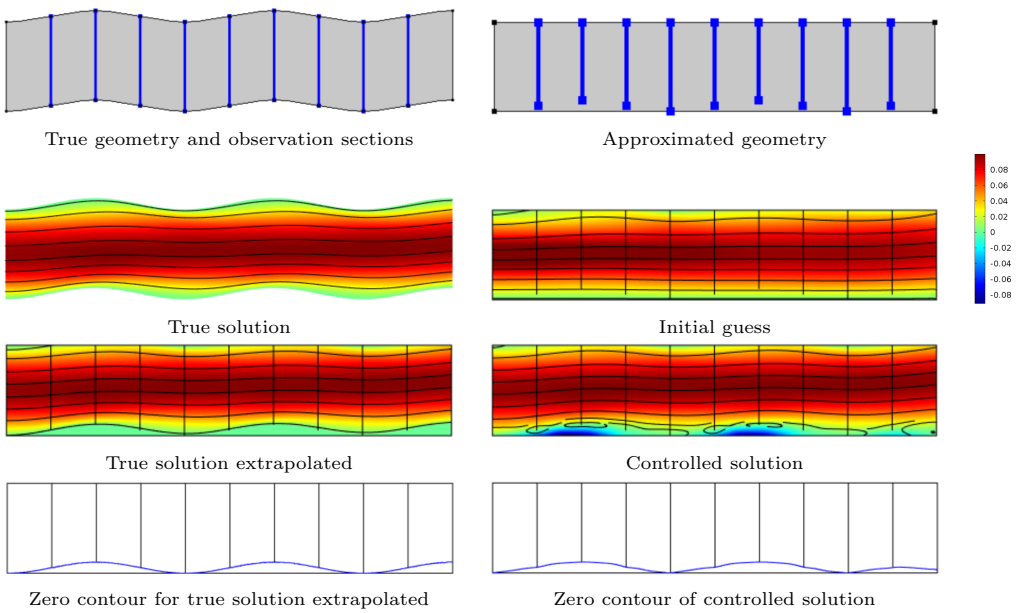

FIGURE 5. Top row left: original geometry with observed sections. Top row right: approximated geometry with observed sections. Second row left: solution for the original geometry. Second row right: approximated solution using constant average velocity. Third row left: solution extrapolated for the approximated geometry. Third row right: controlled solution. Bottom row left: zero contour level in the approximated geometry. Bottom row right: zero contour level of the controlled solution.

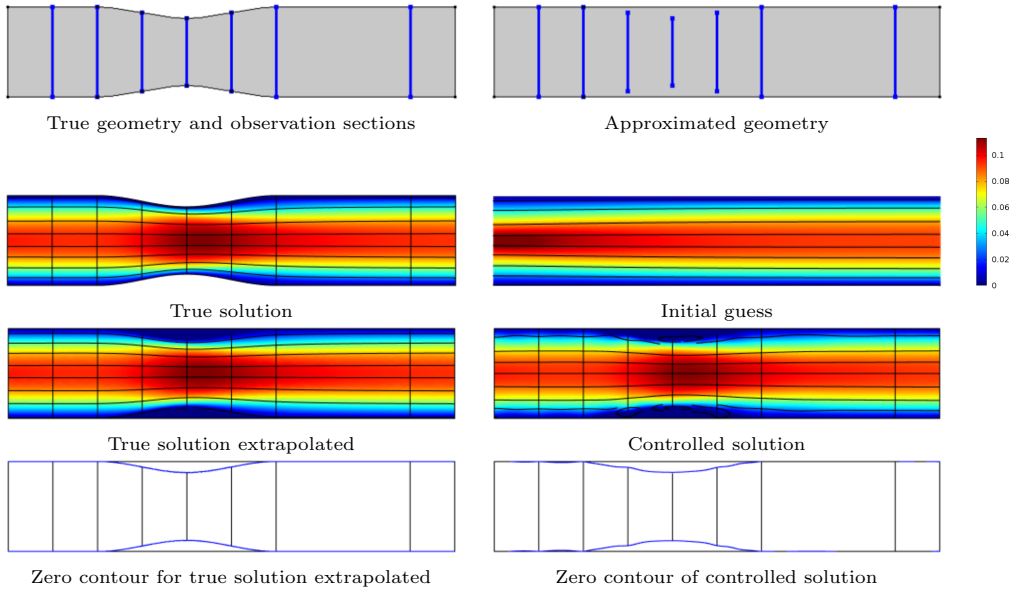

FIGURE 6. Top row left: original geometry with observed sections. Top row right: approximated geometry with observed sections. Second row left: solution for the original geometry. Second row right: approximated solution using constant average velocity. Third row left: solution extrapolated for the approximated geometry. Third row right: controlled solution. Bottom row left: zero contour level in the approximated geometry. Bottom row right: zero contour level of the controlled solution.

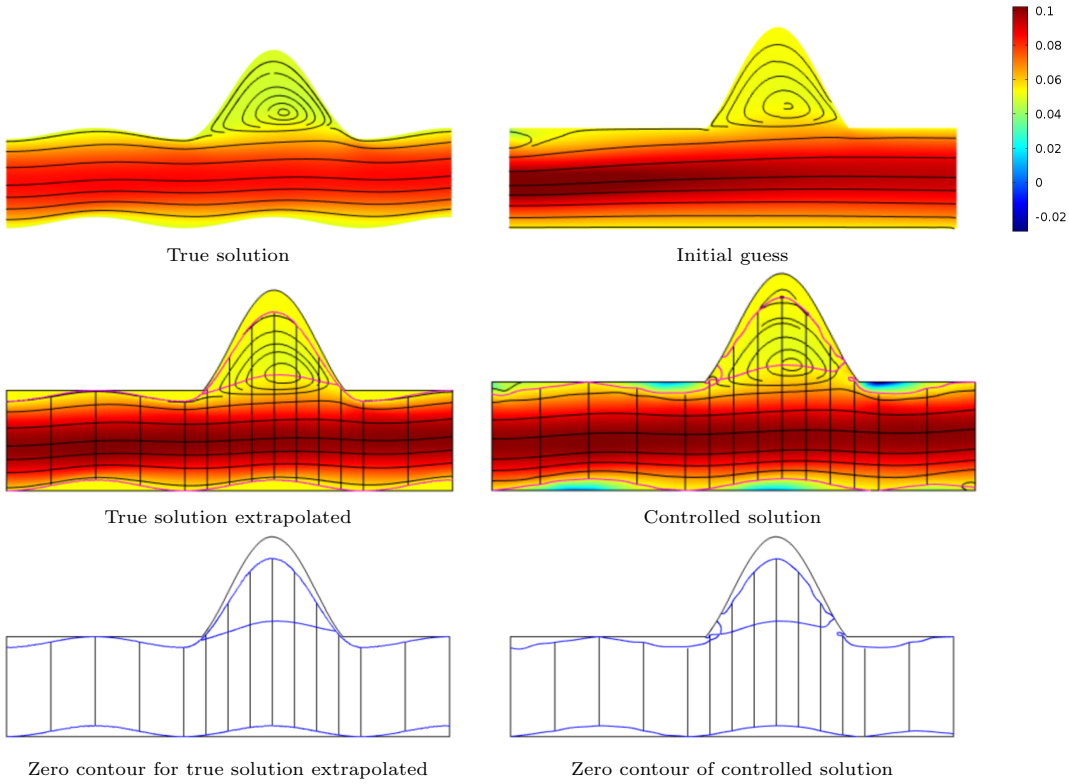

FIGURE 7. Top row left: solution for the original geometry. Top row right: approximated solution using constant average velocity. Middle row left: solution extrapolated for the approximated geometry. Middle row right: controlled solution. Note that the lines in magenta represent the zero contour of the x-component of the velocity. Bottom row left: zero contour level in the approximated geometry. Bottom row right: zero contour level of the controlled solution.

left column on the second row, where the true solution is overlapped). Besides the streamlines we also represent, in magenta, the zero contour for the x-component of the velocity. It corresponds to the no-slip boundary condition, and in the interior of the aneurysm it indicates the location of the reversing flow. The observation sections Ω_{obs} (shown by the black vertical lines) are concentrated within the aneurysm area, due to the big geometry change, the reversed flow and the low magnitude velocity. We also include other sections, covering the full length of the channel, a need that was detailed in Section 4.2. We note that the control function $\mathbf{c}_1$ also describes the velocity vector at the aneurysm wall, which is included in the upper boundary Γ_{c_1}.

The optimal solution recovers the behavior of the true solution, in terms of the streamlines and also for the zero contour of the velocity x-component. We note that the no-slip boundary is accurately recovered, however the definition of the proximal region of the aneurysm neck performs worse due to the limited resolution in distinguishing the geometry wall and the reversed flow boundaries. As noted in Section 4.2, the use of extra observations in this region would yield more precise results.

4.7. A realistic geometry - saccular aneurysm

Finally, we apply our procedure to adjust a reconstructed geometry obtained from a 2D longitudinal section of a saccular aneurysm, inspired from the work of [36] and generated using interpolating splines, as shown in Figure 8. The computational domain involves a single inflow section (on the left) and two outflow sections (upper and lower). The problem set here is to concentrate on the shape and flow within

the aneurysm, since this is clinically the most important feature. The reconstructed geometry Ω matches Ω_0 on all boundaries except on the aneurysm dome, where it is inflated. The blue vertical lines represent the observed sections Ω_{obs} which are concentrated solely in the aneurysm. To recover the flow field in the aneurysm and the no-slip boundary of the dome, we will control a portion of the dome boundary, as highlighted in the bottom-right image, and also the inlet boundary Γ_{in} in a similar way to the example of Section 4.1.

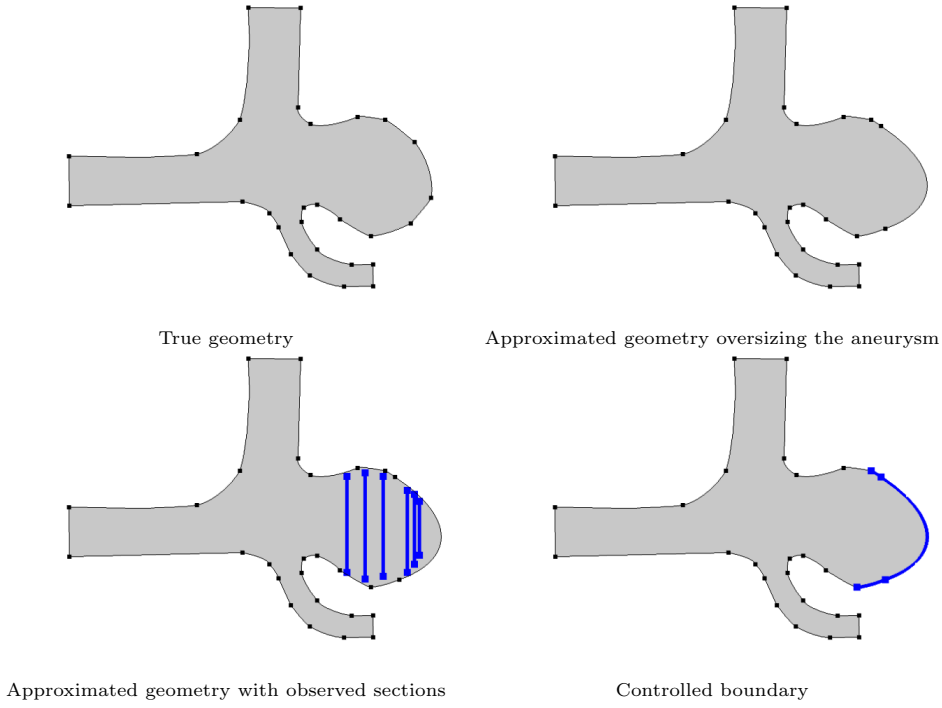

FIGURE 8. Top row left: original geometry. Top row right: approximated geometry. Bottom row left: observation sections Ω_{obs}. Bottom row right: the boundary to be controlled.

The resulting solutions are presented in Figure 9. As above, we use the x-component of the velocity and the streamlines to describe the flow and the no-slip boundary. In this example, the magnitude does not reach zero but rather an approximate value 2×10^{-5} which we use to estimate the location of the no-slip boundary in that area.

Similar to the results in Section 4.6, improvement in the accuracy can be obtained with more observation data, especially near the wall. In fact, in the regions close to the controlled boundary, where the velocity magnitude is very small and there are no observations, the no-slip boundary is not reproduced accurately. This can be seen in Figure 10, where we represent the detail of the streamlines and the magnitude contour for the true solution (left), initial guess (center) and controlled solution (right). We note that the cost function given by equation (2.2) penalizes the misfit of velocities, however if these are small as in a slow recirculating region of an aneurysm, this term has a smaller weight. A normalized misfit cost function could improve the accuracy of the solution.

5. Conclusions and remarks

We have presented an automatic procedure to minimize the difference between measured observations and solutions to numerical simulations. With emphasis on patient-specific computational hemodynamics,

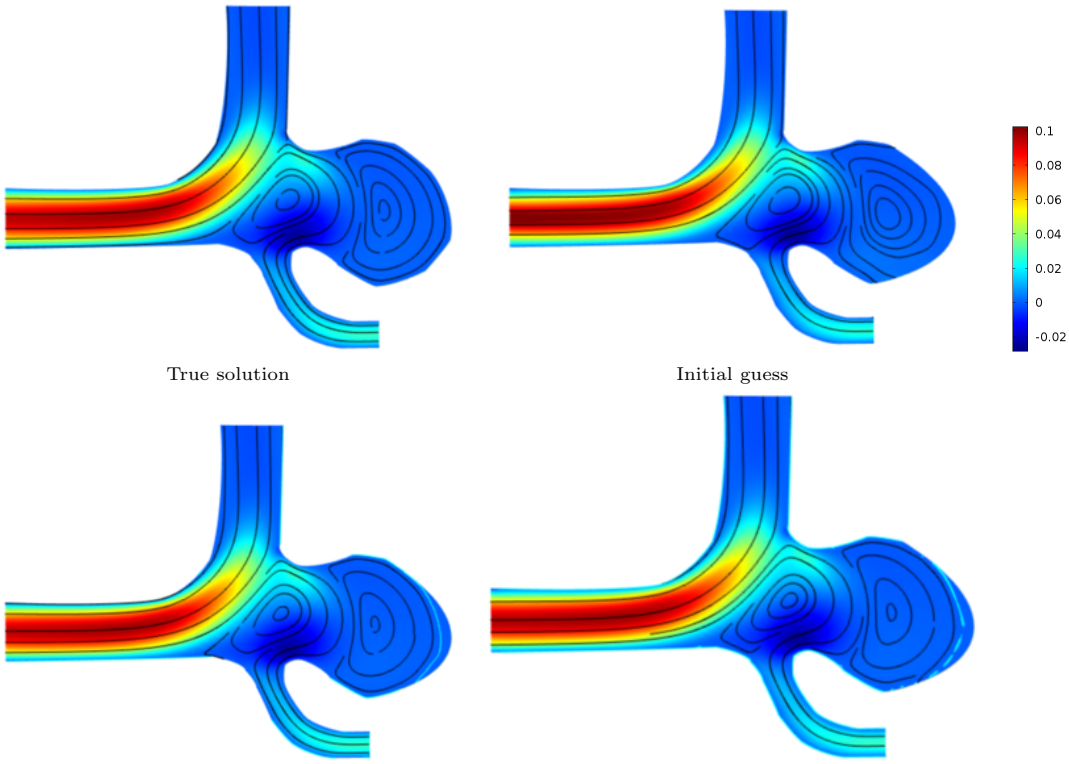

FIGURE 9. Top row left: solution for the original geometry. Top row right: approximated solution using constant average velocity. Bottom row left: solution extrapolated for the approximated geometry. Bottom row right: velocity zero contour of the controlled solution.

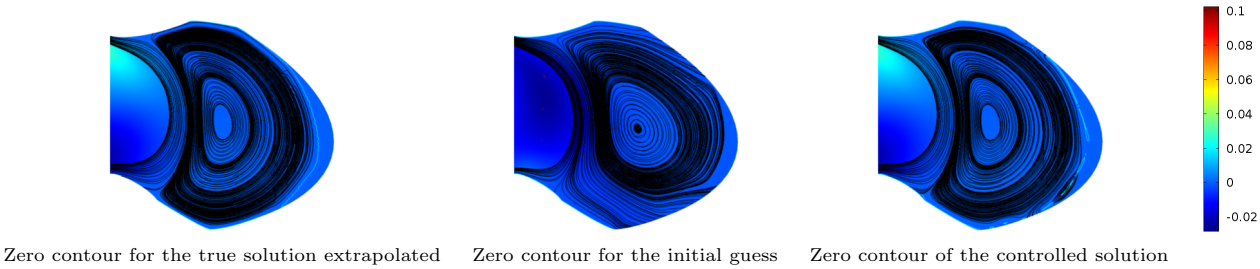

FIGURE 10. Left: streamlines and zero-magnitude velocity for original solution. Center: streamlines for initial guess. Right: streamlines and zero-magnitude velocity for controlled solution.

this tool has been used to correct approximate boundary conditions at the inflow and the definition of the no-slip boundary. In practice, the method is used to minimize the uncertainty that arises due to: i) the correct choice of the boundary conditions at the artificial truncation of the computational domain, ii) the definition of the geometry caused by noisy and limited resolution medical image data.

The measured observations used in the cost minimization are velocity data, that can be obtained from non-invasive phase contrast MRI. These observations should adequately cover the computational domain. They also suffer from artifacts, noise and limited resolution, however the procedure outlined in this work

is shown by means of example cases, to be robust to such noise. A strength of the method is that it is automatic as it does not require any supervision, and guarantees minimal error solution.

The procedure has been validated with various 2D models through numerical tests. Particular attention to the accuracy of the solution has been devoted to the recovery of the true domain's no-slip boundaries. These are sensitive measures of interest since many diseases have been correlated to the wall shear stress. The test cases have included a stenosis geometry with high values of velocity and velocity gradients, and aneurysm geometries, that contain regions of flow separation and flow recirculation. The simulations have been performed for steady state which is often sufficient for practical clinical studies. The proposed method can be extended to the time dependent case, however the computational cost will be greatly increased. Current simulation time requires about 30 min to obtain a relative error smaller than 0.46%, with 800 dofs for the control variable and 14500 dofs for the velocity vector.

At the current stage of the work, there is no criteria for an automatic choice for the location of the observations in the true domain, that can greatly impact on the quality of the obtained results. This is a subject of observability and controllability theory, that was not treated here. This important point, together with exploring other cost functionals to be minimized and an extension to the 3-dimensional case, should be covered in future work.

The proposed method has shown, through the set of numerical test cases, to be useful as an unsupervised method to choose flow boundary conditions and identify a more accurate definition of the geometry no-slip walls. The tools presented can be used to address current concerns in correct numerical simulation definition setup.

Acknowledgements. This work was partially supported by FCT (Portugal) through the Research Center CEMAT-IST, the grant SFRH/BPD/66638/2009, and the project EXCL/MAT-NAN/0114/2012. The second author gratefully acknowledges support from project MatComPhys under the European Research Executive Agency FP7-PEOPLE-2011-IEF framework.

References

[1] F.E. Boas, D. Fleischmann. *CT artifacts: causes and reduction techniques.* Imaging in Medicine, 4 (2012), 229-240.

[2] T. Bodnar, A. Sequeira, M. Prosi. *On the shear-thinning effects of blood flow under various flow rates.* Applied Mathematics and Computation, Elsevier, 217 (2011), 5055-5067.

[3] J. Burkardt, M. Gunzburger, J. Peterson. *Insensitivite Functionals, Inconsistent Gradients, Spurious Minima and Regularized Funcionals in Flow Optimization Problems.* International Journal of Computational Fluid Dynamics, 16 (2002), 171-185.

[4] J.R. Cebral, M.A. Castro, S. Appanaboyina, C.M. Putman, D. Millan, A.F. Frangi. *Efficient pipeline for image-based patient-specific analysis of cerebral aneurism hemodynamics: technique and sensitivity.* IEEE Transactions on Medical Imaging, 344 (2005), 457-467.

[5] COMSOL Multiphysics, Users Guide, COMSOL 4.3, 2012.

[6] Optimization Module, Users Guide, COMSOL 4.3, 2012.

[7] M. D' Elia, M. Perego, A. Veneziani. *A Variational Data Assimilation Procedure for the Incompressible Navier-Stokes Equations in Hemodynamics.* Journal of Scientific Computing, 53 (2011).

[8] M. D' Elia, A. Veneziani. *A Data Assimilation technique for including noisy measurements of the velocity field into Navier-Stokes simulations.* Proceedings of V European Conference on Computational Fluid Dynamics, ECCOMAS, June (2010).

[9] J.C. De Los Reyes, K. Kunisch. *A semi-smooth Newton method for control constrained boundary optimal control of the Navier-Stokes equations.* Nonlinear Anal., 62 (2005), no. 7, 1289-1316.

[10] J.C. De Los Reyes, K. Kunisch. *Optimal control of partial differential equations with affine control constraints.* Control Cybernet., 38 (2009), no. 4, 1217-1249.

[11] J.C. De Los Reyes, Yousept, Irwin. *Regularized state-constraint boundary Optimal control of the Navier-Stokes equations.*, J-Math. Anal. Appl., 356 (2009), no. 1, 257-279.

[12] P. Deuflhard. *A Modified Newton Method for the Solution of Ill-conditioned Systems of Nonlinear Equations with Application to Multiple Shooting.* Numer. Math., 22 (1974), 289-315.

[13] L. Formaggia, J.F. Gerbeau, F. Nobile, A. Quarteroni. *Numerical treatment of defective boundary conditions for the Navier-Stokes equations.* SIAM J. Numer. Anal., 40 (2002) 376-401.

[14] A.M. Gambaruto, D.J. Doorly, T. Yamaguchi. *Wall shear stress and near-wall convective transport: Comparisons with vascular remodelling in a peripheral graft anastomosis*. Journal of Computational Physics, 229 (2010), no. 14, 5339-5356.

[15] A. Garambuto, J. Janela, A. Moura and A. Sequeira. *Sensitivity of hemodynamics in a patient specific cerebral aneurysm to vascular geometry and blood rheology*. Mathematical Biosciences and Engineering, 8 (2011), no. 2, 409-423.

[16] A. Gambaruto, J. Janela, A. Moura, A. Sequeira. *Shear-thinning effects of hemodynamics in patient-specific cerebral aneurysms*. Mathematical Biosciences and Engineering, 10 (2013), no. 3, 649-665.

[17] A.M. Gambaruto, J. Peiro, D.J. Doorly, A.G. Radaelli. *Reconstruction of shape and its effect on flow in arterial conduits*. International Journal for Numerical Methods in Fluids, 57 (2008), no. 5, 495-517.

[18] V. Girault, P.A. Raviart. Finite Element Methods for Navier-Stokes Equations, Theory and Algorithms, Number 5 in Springer Series in Computational Mathematics. Springer-Verlag, Berlin, 1986.

[19] T. Guerra, J. Tiago, A. Sequeira. *Optimal control in blood flow simulations*. International Journal of Non-Linear Mechanics, Available online (2014), doi:10.1016/j.ijnonlinmec.2014.04.005.

[20] M. Gunzburger. *Adjoint Equation-Based Methods for Control Problems in Incompressible, Viscous Flows*. Flow, Turbulence and Combustion, 65 (2000), no. 3, 249-272.

[21] M. Gunzburger, L.S. Hou, T.P. Svobodny. *Analysis and finite element approximation of optimal control problems for the stationary Navier-Stokes equations with Dirichlet controls*. RAIRO - Modélisation mathémathique et analyse numérique, 25 (1991), no. 6, 711-748.

[22] P. Gill, W. Murray, M.A. Saunders. *SNOPT: An SQP Algoritm for Large-Scale Constrained Optimization*. Society for Industrial and Applied Mathematics, SIAM REVIEW, 47 (2005) no. I, 99-131.

[23] B.M. Johnston, P.R. Johnston , S. Corney, D. Kilpatrick. *Non-Newtonian blood flow in human right coronary arteries: transient simulations*. Journal of Biomechanics, 39 (2006), no. 6, 1116-1128.

[24] M. Kroon , G.A. Holzapfel. *Estimation of the distributions of anisotropic, elastic properties and wall stresses of saccular cerebral aneurysms by inverse analysis*. Proc. R. Soc. A, 464 (2008), 807-825.

[25] K.L. Lee, D.J. Doorly, D.N. Firmin. *Numerical simulations of phase contrast velocity mapping of complex flows in an anatomically realistic bypass graft geometry*. Medical Physics, 7 (2006), 2621-2631.

[26] J.G. Myers, J.A. Moore, M. Ojha, K.W. Johnston, C.R. Ethier. *Factors Influencing Blood Flow Patterns in the Human Right Coronary Artery*. Annals of Biomedical Engineering, 29 (2001), no. 2, 109-120.

[27] R.W. Ogden, G. Saccomandi, I. Sgura. *Fitting hyperelastic models to experimental data*. Computational Mechanics, 34 (2004), no. 6, 484-502.

[28] E. Pusey, R.B. Lufkin, R.K. Brown, M.A. Solomon, D.D. Stark, R.W. Tarr, W.N. Hanafee. *Magnetic resonance imaging artifacts: mechanism and clinical significance*. Radiographics, 6 (1986), no. 5, 891-911.

[29] A. Quarteroni, L. Formaggia. Mathematical Modelling and Numerical Simulation of the Cardiovascular System, Modelling of living Systems. Handbook of Numerical Analysis Series. Elsevier, Amsterdam, 2002.

[30] S. Ramalho, A. Moura, A.M. Gambaruto, A. Sequeira. *Sensitivity to outflow boundary conditions and level of geometry description for a cerebral aneurysm*. International Journal for Numerical Methods in Biomedical Engineering, 28 (2012), no. 6-7, 697-713.

[31] A.M. Robertson, A. Sequeira, M.V. Kameneva. *Hemorheology*. Hemodynamical Flows. Modeling, Analysis and Simulation. Oberwolfach Seminars. Birkhauser Verlag, Basel, 37 (2008), 63-120.

[32] O. Schenk, K. Gärtner, W. Fichtner, A. Stricker. *PARDISO: A High-Performance Serial and Parallel Sparse Linear Solver in Semiconductor Device Simulation*, Journal of Future Generation Computers Systems, 18 (2001), 69-78.

[33] T. Silva, A. Sequeira, R. Santos, J. Tiago. *Mathematical Modeling of Atherosclerotic Plaque Formation Coupled with a Non-Newtonian Model of Blood Flow*. Conference Papers in Mathematics, vol. 2013, Article ID 405914, 2013. doi:10.1155/2013/405914.

[34] N.P. Smith, A.J. Pullan, P.J. Hunter. An anatomically based model of coronary blood flow and myocardial mechanics. SIAM J. Appl. Math., 62 (2002), 990-1018.

[35] P. Tricerri. Mathematical and Numerical Modeling of Healthy and Unhealthy Cerebral Arterial Tissue. École Polytechnique Fédérale de Lausanne. Ph.D. thesis, 2014.

[36] Y. Wei, S. Cotin, J. Dequidt, C. Duriez, J. Allard, E. Kerrien. *A (Near) Real-Time Simulation Method of Aneurysm Coil Embolization* http://dx.doi.org/10.5772/48635, INTECH, 2012.

[37] C. Westbrook, C.K. Roth, J. Talbot. MRI in Practice. Wiley-Blackwell, 2011.